



## Article

# Frequency Down-Conversion of Optical Pulse to the Far Infrared and THz Frequency Ranges Due to the Cascading Process in a Medium with a Quadratic Nonlinear Response

Vyacheslav A. Trofimov <sup>1,\*</sup> , Dmitry M. Kharitonov <sup>2</sup>, Mikhail V. Fedotov <sup>2</sup>  and Yongqiang Yang <sup>1</sup><sup>1</sup> School of Mechanical and Automotive Engineering, South China University of Technology, Guangzhou 510641, China; meiqyang@scut.edu.cn<sup>2</sup> Faculty of Computational Mathematics and Cybernetics, Lomonosov Moscow State University, Leninskye Gory, Moscow 119992, Russia; dmitrykharitonov@cs.msu.ru (D.M.K.); fedotov@cs.msu.ru (M.V.F.)

\* Correspondence: trofimov@scut.edu.cn

**Abstract:** Difference-frequency generation is a well-known method of obtaining IR and THz radiation. It has many practical applications, such as sensing, optical metrology, diagnostics, detection and identification of substances, etc. One of the generation methods is based on the three-wave interaction in a medium with second-order nonlinear susceptibility. In this study, we investigated a special case of the frequency down-conversion into IR and THz ranges of the frequencies: the frequencies of interacting waves were multiple. We analyzed theoretically two cases of three-wave interactions: amplification of the infrared (or THz) radiation (incident weak intensity of a wave at this frequency) and a wave generation with the difference-frequency (incident zero-value intensity at this frequency). The amplification efficiency could achieve 75% and the maximal frequency conversion efficiency is about 25%. The computer simulation results made for the femtosecond pulse interaction in a crystal with the wavelength 4, 10, and 24  $\mu\text{m}$  demonstrates applicability of such a scheme for the frequency down-conversion. This scheme of the THz radiation generation is a perspective tool for its application in the screening system for the detection and identification of substances.

**Keywords:** frequency down-conversion; cascading processes; infrared optics; terahertz optics



**Citation:** Trofimov, V.A.; Kharitonov, D.M.; Fedotov, M.V.; Yang, Y.

Frequency Down-Conversion of Optical Pulse to the Far Infrared and THz Frequency Ranges Due to the Cascading Process in a Medium with a Quadratic Nonlinear Response. *Appl. Sci.* **2022**, *12*, 3891. <https://doi.org/10.3390/app12083891>

Academic Editor: Mira Naftaly

Received: 2 March 2022

Accepted: 8 April 2022

Published: 12 April 2022

**Publisher's Note:** MDPI stays neutral with regard to jurisdictional claims in published maps and institutional affiliations.



**Copyright:** © 2022 by the authors. Licensee MDPI, Basel, Switzerland. This article is an open access article distributed under the terms and conditions of the Creative Commons Attribution (CC BY) license (<https://creativecommons.org/licenses/by/4.0/>).

## 1. Introduction

Infrared optics and THz optics have various practical applications, including spectroscopy [1,2], optical metrology [3], material measurements [4], sensing [5], diagnostics, detection, identification of substances, etc. One of the possible ways to obtain laser radiation in these ranges of the frequencies is via a frequency down-conversion process, due to the difference frequency's wave generation in a medium with a quadratic nonlinear response.

The difference frequency's wave generation, whose frequency belonging to an infrared frequencies range, has attracted the attention of many researchers. Below, we mention some of them. In [6], the femtosecond pulses with tunable wavelengths belonging to the interval (3.2–4.8  $\mu\text{m}$ ), and possessing a maximal average power of about 1.1 mW, were generated in the MgO:LiNbO<sub>3</sub> crystal. In [7], a tunable source of the mid-infrared CW radiation with a maximal power of 51 mW at a wavelength  $\lambda_1 = 6543$  nm was created based on the difference frequency's wave generation in a GaAs crystal. Optical frequency combs with wavelengths belonging to their intervals (2.8–3.5  $\mu\text{m}$ ) were generated in MgO:PPLN crystal using the difference frequency's wave generation [8]; a similar result was also obtained in GaSe crystal with the frequency combs generation, in the wavelength range 3–10  $\mu\text{m}$  [9].

Frequency down-conversion also consists of using the optical parametric oscillation process. Thus, in [10], by using this tool, a conversion efficiency of 34% was achieved with the average output power of 7.7 W at the power of the incident pump pulse equal to 23 W. The IR radiation at a wavelength 7  $\mu\text{m}$  with an energy of 0.71 mJ was obtained

with a 7.8% quantum conversion efficiency in BaGa<sub>4</sub>Se<sub>7</sub> crystal [11]. Tunable IR radiation generation belonging to the wavelength range 4.4–5.7 μm, with a maximal output energy of 13.1 μJ, was achieved in [12], using La<sub>3</sub>Ga<sub>5.5</sub>Nb<sub>0.5</sub>O<sub>14</sub> crystal. A review of the frequency down-conversion processes in non-oxide media can be found in [13].

A THz radiation source using difference-frequency generation was also obtained in many nonlinear media. For example, a THz pulse with the wavelength in the range of 290–140 μm was realized in a LiNbO<sub>3</sub> crystal [14]. The periodically-poled LiNbO<sub>3</sub> crystal was used in [15], the frequency range was 1.5–1.8 THz; a maximal power was equal to 0.1 mW; and in [16], the wavelength range was 190–210 μm and 457–507 μm; the maximal energies were equal to 0.37 and 0.057 pJ, respectively; in [17], the authors explored the realization of a generation scheme of the difference-frequency equal to 0.5 THz with a conversion efficiency of 30%.

It should be noted that, in a series of studies, i.e., [18–21] and the corresponding references listed in those papers, the THz radiation with a wavelength range of 66.5 μm, 5664 μm was obtained in crystals GaSe, ZnGeP<sub>2</sub> GaP based on difference frequency's wave generation with conversion efficiency equal to 0.1%.

Crystal ZnTe is often used for frequency down-conversion to obtain a THz radiation. We can note, for example, the following papers: [22], where pulse 1 THz was obtained as 365 and 364 THz frequency differences and with a 0.6% conversion efficiency. In Reference [23], the authors demonstrated the possibility of pulse generation with tunable frequency, in the range of 0.3–2.5 THz, and power up to 1 μW based on difference-frequency generation involving interactions of picosecond pulses, with intensity at  $2.58 \times 10^8$  W/cm<sup>2</sup> generated with 1.5% conversion efficiency.

In another THz pulse source with tunable frequency, the frequency range was 0.3–19.6 THz, with energy at 870 nJ, and was obtained in the DAST crystal lit by an incident pulse with a power density of 247 MW/cm<sup>2</sup> [24]. Using a GaSe crystal with a length of 8 mm and a down-conversion frequency process, a source of the tunable frequency, belonging to a frequency range of 0.21–3 THz, and conversion efficiency equal 0.00168%, was created [25]. A review of the sources of the THz radiation based on the frequency down-conversion process is presented in [26]. In turn, a review of quantum cascade lasers using the the difference-frequency generation process for obtaining THz radiation is found in [27]. It should be noted that a process of the difference-frequency generation was also used for developing THz CW spectrometers based on lithium niobate channel-waveguides [28], which is important regarding the problem of substance detection and identification.

A crystal AgGaS<sub>2</sub> is widely used for IR radiation generation [29–33]. IR radiation generation with wavelength intervals at 3.9 μm and 9.4 μm, at incident pulse durations in picosecond ranges, was discussed in [29]. The achieved conversion efficiency of the energy transform was a few percent for the incident pulse energy of 10 mJ. The difference-frequency generation was chosen as a base of the IR spectrometer [30]. The pulses possessing the energy (10 μJ) and duration (50 ns), and wavelength intervals at 3–12 μm, were obtained in [31]. The femtosecond pulse interaction scheme used for obtaining pulses with a tunable frequency in the mid-infrared range and output energy, equaling several mJ, was discussed in [32]. The source of pulses, constructed using the difference-frequency generation with the efficiency 0.6%, with tunable wavelength intervals at 5–12 μm, and a duration 8 ns, was presented in [33].

In past years, the frequency up-conversion in the tellurium chains have been widely discussed (see, for example, [34]); thus, one may expect the frequency down-conversion process in this crystal will be effective. The tellurium crystal has a big transmittance range in the infrared range of the wavelengths (at least until 24 μm, according to [35]), and a large second-order susceptibility [36]. The frequency down-conversion to the range of the mid-infrared frequencies with a peak power of 100 μW, achieved in tellurium crystal with a length 11 μm, is presented in [37].

In the current study, we propose a new approach for the frequency down-conversion to infrared (or even THz) range using the difference-frequency generation at wave interactions with multiple frequencies  $\omega$  (low-frequency wave, LFW),  $2\omega$  (intermediate frequency wave, IFW),  $3\omega$  (high-frequency wave, HFW), in the case of large phase-mismatching between two interacting waves. To our knowledge, such a scheme, regarding the frequency down-conversion, has not been discussed in previous literature. We present the computer simulation results for the frequency down-conversion of femtosecond pulses, with duration equal to 100 fs for the pulses with corresponding wavelengths,  $4\ \mu\text{m}$  (75 THz),  $10\ \mu\text{m}$  (50 THz; belongs to the infrared frequencies range), and  $24\ \mu\text{m}$  (12.5 THz; belongs to the THz frequencies range), if the LFW and HFW interact in the phase-matched mode and the phase mismatching between IFW and LFW is large enough. Therefore, it allowed us to apply the multi-scale method to derive the modified set of equations and to solve those equations analytically in the long pulse duration approximation framework and plane wave approximation, but without using the energy non-depletion approximation of HFW.

The computer simulation is provided for two well-known crystals—AgGaS<sub>2</sub> and tellurium. Our calculations, based on the results of the Sellmeier equations, taken from study [38], show that it is possible to achieve phase matching between LFW and HFW in this crystal at the LFW wavelength, up to  $10\ \mu\text{m}$  in the crystal AgGaS<sub>2</sub>. Thus, we use this crystal’s data for the frequency down-conversion into the radiation possessing wavelength equal to  $4\ \mu\text{m}$  and  $10\ \mu\text{m}$ , and the tellurium crystal data [39] for the frequency down-conversion to wavelength  $24\ \mu\text{m}$ .

Our paper is organized as follows. We begin with the set of nonlinear Schrödinger equations accounting for the group velocity dispersion (GVD) of the laser pulses. Then, based on the multi-scale method, we derive the modified set of equations and solve them without using the energy non-depletion approximation for HFW in the framework of the long pulse duration approximation. This solution demonstrates that the effective energy conversion of HFW to LFW is possible, even if the incident IFW’s intensity is small.

The latter part of our study contains computer simulation results, showing how GVD influences energy conversion efficiency. That section is divided into two parts: investigation of the amplification process (small incident LFW’s intensity) and the generation process (incident LFW’s intensity is equal to zero). In both cases, we demonstrate that a highly-effective frequency down-conversion process occurs under certain conditions.

## 2. Problem Statement

The three-wave interaction process with multiple frequencies in a medium with quadratic nonlinear responses can be described by the set of nonlinear Schrödinger equations [40]:

$$\begin{aligned} \frac{\partial A_1}{\partial z} + iD_1 \frac{\partial^2 A_1}{\partial t^2} + i\left(\gamma_{12}A_1^*A_2e^{-i\Delta_{21}kz} + \gamma_{23}A_2^*A_3e^{-i(\Delta_{31}k-\Delta_{21}k)z}\right) &= 0, \\ \frac{\partial A_2}{\partial z} + \nu_{21} \frac{\partial A_2}{\partial t} + iD_2 \frac{\partial^2 A_2}{\partial t^2} + i\left(\gamma_{11}A_1^2e^{i\Delta_{21}kz} + 2\gamma_{13}A_1^*A_3e^{-i(\Delta_{31}k-\Delta_{21}k)z}\right) &= 0, \\ \frac{\partial A_3}{\partial z} + \nu_{31} \frac{\partial A_3}{\partial t} + iD_3 \frac{\partial^2 A_3}{\partial t^2} + 3i\gamma_{21}A_1A_2e^{i(\Delta_{31}k-\Delta_{21}k)z} &= 0, \quad 0 < z \leq L_z, \quad 0 < t < L_t. \end{aligned} \tag{1}$$

The initial condition and boundary conditions (BCs) are the following:

$$\begin{aligned} A_1(0, t) = A_{10}(t), \quad A_2(0, t) = A_{20}(t), \quad A_3(0, t) = A_{30}(t), \quad t \in [0, L_t], \\ A_1(z, 0) = A_2(z, 0) = A_3(z, 0) = A_1(z, L_t) = A_2(z, L_t) = A_3(z, L_t) = 0, \quad z \in [0, L_z], \end{aligned} \tag{2}$$

which correspond to the absence of the laser radiation of all optical waves out of a certain time interval. Here,  $A_j$  are dimensionless complex amplitudes of LFW, IFW, and HFW. Coefficients  $\gamma_{jk}$ —of nonlinear coupling of interacting waves—characterize a second-order nonlinear response at the corresponding frequencies. Below, for simplicity, we omit a dependence of this coefficient on the optical frequency. Therefore, these coefficients are

equal to the same value:  $\gamma_{jk} = \gamma$ . We emphasize that this is not a strong restriction for our analysis. Parameters  $\Delta_{21}k$  and  $\Delta_{31}k$  denote dimensionless phases mismatching between IFW and LFW, and HFW and LFW, respectively. Coefficients  $\nu_{21}$  and  $\nu_{31}$  are dimensionless mismatching of the group velocities between pulses of IFW and LFW, and HFW and LFW, respectively. Parameters  $D_1$ ,  $D_2$  and  $D_3$  are dimensionless coefficients of the second order dispersion (SOD) at the corresponding frequencies, characterizing GVD of the propagating pulses.  $t$  and  $z$  are dimensionless time and space coordinates, correspondingly.

Let us note that the diffraction is not taken into account in Equation (1). This is valid if the radii of the incident beams are large enough to satisfy the following conditions: the diffraction length is greater than the crystal’s length and the nonlinear length, which is defined by the incident beam’s maximal intensity. Such conditions often occur in physical experiments (see, for example, [41–43]). Writing Equation (1), we neglected the cubic nonlinear response of a crystal. It can be done if the maximal intensity of the incident pulse is less than the certain value, depending on the used crystal [40].

The dimensionless variables and parameters are expressed through the physical ones as follows:

$$\begin{aligned} \nu_{j1} &= \left( \frac{\partial \bar{k}}{\partial \bar{\omega}} \Big|_{\bar{\omega}_j} - \frac{\partial \bar{k}}{\partial \bar{\omega}} \Big|_{\bar{\omega}_1} \right) \frac{Z_n}{\tau_p}, \quad j = 2, 3, \quad D_j = -\frac{1}{2} \frac{\partial^2 \bar{k}}{\partial \bar{\omega}^2} \Big|_{\bar{\omega}_j} \frac{Z_n}{\tau_p^2}, \quad A_j = \frac{\bar{A}_j}{A_0}, \quad j = 1, 2, 3, \\ \gamma &= \frac{2\pi\chi^{(2)}\bar{k}_1 A_{01}}{n^2} Z_n, \quad \Delta_{21}k = \Delta_{21}\bar{k}Z_n, \quad \Delta_{31}k = \Delta_{31}\bar{k}Z_n. \end{aligned} \tag{3}$$

where  $\tau_p$  is the incident pulse duration of the LFW ( $\bar{\omega}_1 = \bar{\omega}$ ), which is chosen to be equal to 100 fs, if we do not specify otherwise. Time coordinates are measured in  $\tau_p$ . Parameter  $Z_n$  is a normalization length chosen equal 1 mm. The propagation distance of the optical pulse is measured in this units. Coefficients  $\chi^{(2)}(\bar{\omega}_j, \bar{\omega}_l)$  are the quadratic susceptibilities of a medium at the frequencies  $\bar{\omega}_j, \bar{\omega}_l$ . The frequency  $\bar{\omega}_j = j\bar{\omega}$  is associated with the wavelength  $\lambda_j$  by the known ratio:  $\bar{\omega}_j = 2\pi c/\lambda_j, j = 1, 2, 3$ . Parameter  $\bar{k}_1$  is a dimensional wave-number of the LFW. In turn,  $\Delta_{21}\bar{k}$  and  $\Delta_{31}\bar{k}$  are dimensional phases mismatching between the IFW or the HFW and the LFW, respectively:  $\Delta_{j1}\bar{k} = \bar{k}_j - j\bar{k}_1, j = 2, 3$ . Parameters  $\bar{k}_2, \bar{k}_3$  are the wavenumbers at the frequencies  $\bar{\omega}_2, \bar{\omega}_3$ , respectively. Variables  $\bar{A}_j$  are the complex envelopes of the wave packets measured in physical units.  $A_0$  is a normalization value, which is chosen as the squared root of the LFW and HFW intensities sum at their pulse centers.

In Table 1, we present the physical parameters at various frequencies in a dependence of the wavelength of LFW (4, 10, and 24  $\mu\text{m}$ , respectively). These values were used in the computer simulation and can be used for the arrangement of the physical experiment.

**Table 1.** Characteristics of nonlinear crystal.

$\lambda_1$	$I_0$ (GW/cm <sup>2</sup> )	$\theta$ (°)	$\frac{d^2\bar{k}}{d\bar{\omega}^2} \Big _{\omega=\omega_1}$ (m <sup>-1</sup> s <sup>2</sup> )	$\frac{d^2\bar{k}}{d\bar{\omega}^2} \Big _{\omega=\omega_2}$ (m <sup>-1</sup> s <sup>2</sup> )	$\frac{d^2\bar{k}}{d\bar{\omega}^2} \Big _{\omega=\omega_3}$ (m <sup>-1</sup> s <sup>2</sup> )
4 $\mu\text{m}$ (AgGaS <sub>2</sub> , [38])	6.12	49.46	$4 \times 10^{-27}$	$2.5 \times 10^{-25}$	$4.34 \times 10^{-25}$
10 $\mu\text{m}$ (AgGaS <sub>2</sub> , [38])	20.66	79.51	$-3.2 \times 10^{-24}$	$-1.51 \times 10^{-24}$	$-8.28 \times 10^{-25}$
24 $\mu\text{m}$ (Te, [39])	0.11	15.78	$-4.36 \times 10^{-24}$	$1.58 \times 10^{-24}$	$3.08 \times 10^{-24}$

Among them, we also present the angle  $\theta$  between the laser pulse propagation direction and the crystal axis, at which the phase matching between the LFW and HFW occurs (so we assume that  $\Delta_{31}k = 0$ ). We also present the sum incident intensity of the LFW and HFW  $I_0$ , at which the parameter  $\gamma$  equals unity. This choice is explained by our further analysis. It should be noted that the phase mismatching between the IFW and LFW is partly defined by the condition  $\Delta_{31}k = 0$ . Thus, the phase matching angle  $\theta$  and the phase mismatching are computed on the basis of Sellmeier equations, taken from [38,39], using the formulas that can be found, for example, in [40] (paragraph 2.3).

Below, we also neglect the group velocity mismatching:  $v_{21} = v_{31} = 0$  to clarify the SOD influence on the frequency conversion efficiency. This imposes certain restrictions on the crystal length and the pulse durations, which should be large enough to avoid the running away from each other at the output face of the crystal. If the pulse duration is about 1 ps, then such a length can achieve a value about a few dozens of centimeters. If the pulse duration is about 100 fs, then the group velocity mismatching does not essentially influence the conversion efficiency, until ten centimeters of the optical pulse propagation distance. It only changes the pulse shapes by making them asymmetric.

### 3. Modified Equations Derived in the Framework of the Multi-Scale Method

#### 3.1. Set of Modified Equations

If the phase mismatching between LFW and IFW is much larger than the nonlinear coefficient ( $|\Delta_{21}k| \gg \gamma$ ), we can derive the qualitative approximation of the problem (1), (2) solution using the multi-scale method:

$$\begin{aligned} A_1 &= U + \frac{1}{\Delta_{21}k} \left( \gamma(U^*V e^{-i\Delta_{21}kz} - V^*W e^{i\Delta_{21}kz}) + u_1 \right), \\ A_2 &= V + \frac{1}{\Delta_{21}k} \left( -\gamma(U^2 + 2U^*W) e^{i\Delta_{21}kz} + v_1 \right), \\ A_3 &= W + \frac{1}{\Delta_{21}k} \left( 3\gamma UV e^{-i\Delta_{21}kz} + w_1 \right), \end{aligned} \tag{4}$$

with accuracy of  $O(\Delta_{21}k^{-2})$ . Here, the functions  $U, V, W$  are governed by the following set of equations:

$$\begin{aligned} \frac{\partial U}{\partial z} + iD_1 \frac{\partial^2 U}{\partial t^2} - i\tilde{\alpha}(|U|^2U + 3U^*W - 4U|V|^2 + 2U|W|^2) &= 0, \\ \frac{\partial V}{\partial z} + v_{21} \frac{\partial V}{\partial t} + iD_2 \frac{\partial^2 V}{\partial t^2} + 2i\tilde{\alpha}(4|U|^2 - |W|^2)V &= 0, \\ \frac{\partial W}{\partial z} + v_{31} \frac{\partial W}{\partial t} + iD_3 \frac{\partial^2 W}{\partial t^2} - 3i\tilde{\alpha}(U^3 + 2|U|^2W + |V|^2W) &= 0, \end{aligned} \tag{5}$$

where  $\tilde{\alpha} = \gamma^2 / \Delta_{21}k$ . The functions  $u_1, v_1, w_1$  are the solutions of the following linear equations:

$$\begin{aligned} \frac{\partial u_1}{\partial z} + iD_1 \frac{\partial^2 u_1}{\partial t^2} &= 0, \\ \frac{\partial v_1}{\partial z} + v_{21} \frac{\partial v_1}{\partial t} + iD_2 \frac{\partial^2 v_1}{\partial t^2} &= 0, \\ \frac{\partial w_1}{\partial z} + v_{31} \frac{\partial w_1}{\partial t} + iD_3 \frac{\partial^2 w_1}{\partial t^2} &= 0. \end{aligned} \tag{6}$$

Let us note that the derivation of these equations is made in Appendix A. The distributions for the new functions corresponding to the complex amplitudes of the incident pulses are the following:

$$\begin{aligned} U(0, t) &= A_{10}(t), \quad V(0, t) = A_{20}(t), \quad W(0, t) = A_{30}(t), \\ u_1(0, t) &= \gamma(A_{20}^*(t)A_{30}(t) - A_{10}^*(t)A_{20}(t)), \quad v_1(0, t) = \gamma(A_{10}^2(t) + 2A_{10}^*(t)A_{30}(t)), \\ w_1(0, t) &= -3\gamma A_{10}(t)A_{20}(t), \quad t \in [0, L_t], \\ U(z, 0) &= V(z, 0) = W(z, 0) = U(z, L_t) = V(z, L_t) = W(z, L_t) = 0, \\ u_1(z, 0) &= v_1(z, 0) = w_1(z, 0) = u_1(z, L_t) = v_1(z, L_t) = w_1(z, L_t) = 0, \quad z \in [0, L_z]. \end{aligned} \tag{7}$$

The set of Equation (5) possesses some conservation laws (invariants):

$$\begin{aligned}
 I_{1UW} &= \int_0^{L_t} (|U|^2 + |W|^2) dt = const, \\
 I_{1V} &= \int_0^{L_t} |V|^2 dt = const, \\
 I_3 &= \int_0^{L_t} \left( 3v_{21} \operatorname{Im} \left( V^* \frac{\partial V}{\partial t} \right) + 2v_{31} \operatorname{Im} \left( W^* \frac{\partial W}{\partial t} \right) - 6D_1 \left| \frac{\partial U}{\partial t} \right|^2 - 3D_2 \left| \frac{\partial V}{\partial t} \right|^2 - 2D_3 \left| \frac{\partial W}{\partial t} \right|^2 \right. \\
 &\quad \left. - 3\tilde{\alpha} \left( 4\operatorname{Re}(U^3 W^*) + |U|^4 + 4|U|^2 |W|^2 - 8|U|^2 |V|^2 + 2|V|^2 |W|^2 \right) \right) dt = const.
 \end{aligned}
 \tag{8}$$

These invariants show that, in the framework of the modified equations, the energy exchanges occur only between LFW and HFW. Meanwhile, the IFW energy remains constant. This fact explains why we choose the normalization value  $A_0$  in (3) as the square root from the sum of the intensities of LFW and HFW achieved at the pulse center.

### 3.2. Frequency Down-Conversion in the Framework of the Long Pulse Duration Approximation

Although our primary goal was to analyze a process of the frequency down-conversion, accounting for SOD, we will briefly present an analysis of this process using the long pulse duration approximation. It allowed us to estimate maximal conversion efficiency.

Let us suppose that the SOD coefficients are equal to zero:  $D_j = 0, j = 1, 2, 3$ . Thus, the functions  $U, V, W$  depend only on  $z$ —coordinate. In this case, the problem (5), (7) can be rewritten as follows:

$$\begin{aligned}
 \frac{dU}{dz} - i\tilde{\alpha}(|U|^2 U + 3U^*{}^2 W - 4U|V|^2 + 2U|W|^2) &= 0, \\
 \frac{dV}{dz} + 2i\tilde{\alpha}(4|U|^2 - |W|^2)V &= 0, \\
 \frac{dW}{dz} - 3i\tilde{\alpha}(U^3 + 2|U|^2 W + |V|^2 W) &= 0, \\
 U(0) = A_{10}, V(0) = A_{20}, W(0) = A_{30}.
 \end{aligned}
 \tag{9}$$

The conservation laws (8) transform in the following way:

$$\begin{aligned}
 I_{1UW} &= |U|^2 + |W|^2 = 1, \\
 I_{1V} &= |V|^2 = |A_{20}|^2, \\
 I_3 &= -3\tilde{\alpha} \left( 4\operatorname{Re}(U^3 W^*) + |U|^4 + 4|U|^2 |W|^2 - 8|U|^2 |V|^2 + 2|V|^2 |W|^2 \right) = const.
 \end{aligned}
 \tag{10}$$

The energy invariant  $I_{UW}$  is chosen equal to unity, for definiteness. This invariant’s choice leads to more simple formulas for LFW generation/amplification efficiency. In general, this value is easy to realize by renormalization of the complex amplitudes.

The Equation (9) can be reduced to a single differential equation. For this aim, we represent the complex amplitudes in a standard way:

$$U(z) = a_1(z) \exp i\varphi_1(z), V(z) = a_{20} \exp(i\varphi_2(z)), W(z) = a_3(z) \exp(i\varphi_3(z)), \tag{11}$$

here, the functions  $a_j, \varphi_j, j = 1, 2, 3$  are real-valued functions. We notice that an equality of  $a_{20} = |A_{20}|$  takes place because of the IFW energy preservation. Thus, the problem (9) takes the form

$$\begin{aligned}
 \frac{da_1}{dz} &= -3\tilde{\alpha}a_1^2a_3 \sin \varphi, \\
 \frac{da_3}{dz} &= 3\tilde{\alpha}a_1^3 \sin \varphi, \\
 \frac{d\varphi}{dz} - \tilde{\alpha} \left( 3 \left( \frac{a_1^3}{a_3} - 3a_1a_3 \right) \cos \varphi + 3a_1^2 - 6a_3^2 + 15a_{20}^2 \right) &= 0, \\
 \frac{d\varphi_2}{dz} + 2i\tilde{\alpha}(4a_1^2 - a_3^2) &= 0, \\
 a_1(0) = |A_{10}|, a_3(0) = |A_{30}|, \varphi(0) = \varphi_0, \varphi_2(0) = \arg(A_{20}). &
 \end{aligned}
 \tag{12}$$

Here,  $\varphi = \varphi_3 - 3\varphi_1$  is a phase difference between HFW and LFW,  $\varphi_0$  is its value in the input section of a medium. Obviously, the invariants (10) are transformed to a form:

$$\begin{aligned}
 I_{1_{a_1 a_3}} &= a_1^2 + a_3^2 = 1, \\
 I_{1_{a_2}} &= a_2^2 = a_{20}^2, \\
 I_3 &= 3\tilde{\alpha} \left( -4a_1^3a_3 \cos \varphi - a_1^4 - 4a_1^2a_3^2 + 8a_{20}a_1^2 - 2a_{20}^2a_3^2 \right).
 \end{aligned}$$

To write the algebraic equation with respect to the phase difference, we modify Hamiltonian by dividing it on  $3\tilde{\alpha}$ :

$$\tilde{I}_3 = -4a_1^3a_3 \cos \varphi - a_1^4 - 4a_1^2a_3^2 + 8a_{20}a_1^2 - 2a_{20}^2a_3^2 = \tilde{I}_{30}
 \tag{13}$$

Thus, we can express  $\cos \varphi$  from the Hamiltonian (13):

$$\cos \varphi = \frac{2a_{20}^2(4a_1^2 - a_3^2) - \tilde{I}_{30} - a_1^4 - 4a_1^2a_3^2}{4a_1^2a_3^2}
 \tag{14}$$

Substituting the expression (14) into the first equation of the set (12), we obtain the equation with respect to the LFW amplitude  $a_1$ :

$$\frac{da_1}{dz} = \mp \tilde{\alpha} a_1^2 a_3 \sqrt{1 - \frac{(2a_{20}^2(4a_1^2 - a_3^2) - \tilde{I}_{30} - a_1^4 - 4a_1^2a_3^2)}{16a_1^6a_3^2}}.$$

Multiplying both parts of the equation on  $a_1$ , and using a new notation  $p_1 = a_1^2$  (it means the LFW intensity), we write the differential equation with respect to the intensity of the LFW  $p_1$ , accounting for an equality  $a_3^2 = 1 - p_1$ :

$$\begin{aligned}
 \frac{dp_1}{dz} &= \mp 7.5\tilde{\alpha} \sqrt{f(p_1)}, \\
 f(p_1) &= -p_1^4 + (0.64 + 0.48B)p_1^3 + (0.24A - 0.16B^2)p_1^2 - 0.16ABp_1 - 0.04A^2, \\
 A &= \tilde{I}_{30} + 2a_{20}^2, B = 2 - 5a_{20}^2.
 \end{aligned}
 \tag{15}$$

The maximal LFW intensity is defined by the roots of the equation  $f(p_1) = 0$ . As neither parameter  $A$  nor parameter  $B$  depend on  $\gamma$  and  $\Delta_{21}k$ , the maximal LFW intensity depends only on the incident intensities of interacting waves. Obviously the nonlinear coupling coefficient and phase mismatching  $\Delta_{21}k$  influence only on a distance on which the maximal LFW intensity achieves.

Since we want to choose the intensity of incident LFW that is as small as possible, the function  $p_1(z)$  should achieve its minimum in section  $z = 0$ . Therefore, its derivative must be equal to zero. As follows from the first Equation (12), this means either  $\varphi_0 = 0$  or  $\varphi_0 = \pi$ . Under this assumption, we solve the equation  $f(p_1) = 0$  for various values  $|A_{10}|^2$ ,  $|A_{20}|^2$  and depict the results of the computation on the plane  $(|A_{10}|^2, |A_{20}|^2)$  (Figure 1).

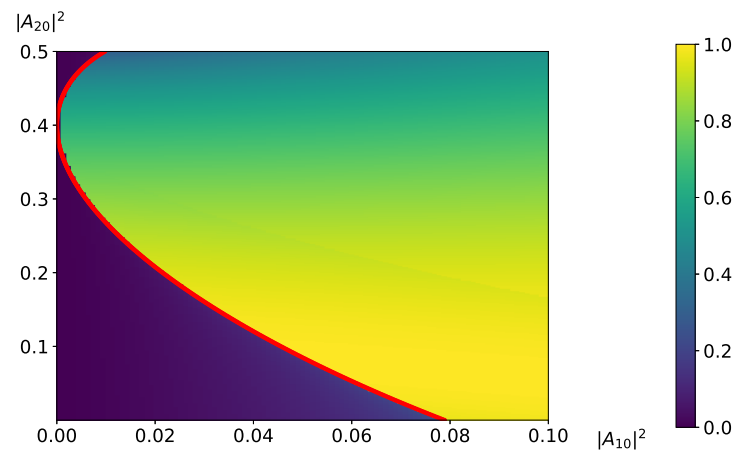


**Figure 1.** The LFW maximal intensity dependence on the incident LFW intensity and the incident IFW intensity. The boundary of domains corresponding to the high-effective and low-effective modes is depicted with a red solid line.

Thus, one can see that there are two regimes of the frequency conversion: low-efficient and high-efficient. In the first one, the conversion efficiency is lower than 20%; in the second one, the conversion efficiency is much higher and can be higher than 90%. We could also see in Figure 1 that if the intensity of incident IFW equals zero then the intensity of incident LFW must be greater or equal than 0.08:  $|A_{10}|^2 \geq 0.08$  to achieve the high-efficiency mode of the frequency conversion. Thus, in accordance with data from Table 1, the following incident intensities of the LFW and HFW are enough for the high-efficient amplification of the pulse with the 4  $\mu\text{m}$  wavelength: 0.4976  $\text{GW}/\text{cm}^2$  and 5.7224  $\text{GW}/\text{cm}^2$ . If the intensity of incident LFW is lower, then the amplification efficiency decreases significantly.

However, with the increasing incident of the IFW intensity, the incident LFW intensity that is required to achieve the high-efficiency mode of the frequency conversion decreases. Moreover, if the incident IFW intensity is equal to  $|A_{20}|^2 = 0.4$ , then the high-efficiency mode occurs even for a zero-value of the incident LFW intensity. The IFW and HFW incident intensities, corresponding to these dimensionless values, can be the following: 2.488  $\text{GW}/\text{cm}^2$  and 6.22  $\text{GW}/\text{cm}^2$ .

It should be noted that the computer simulation results obtained by solving the original problem mostly support this analysis provided on the basis of the modified equations. In particular, two different modes of the frequency conversion also occur if we describe the laser pulse interactions in the framework of the original problem (1).

#### 4. Computer Simulation Results

To confirm the results, discussed in the previous paragraph, the computer simulation results obtained on the basis of solving the problem (1), are presented below. The red solid lines refer to LFW; the blue solid lines refer to IFW; the green solid lines refer to HFW; the black solid lines with triangles denote the incident LFW intensity; the black dashed-dotted lines denote the IFW intensity; the black dashed lines denote the incident HFW intensity. We also placed numbers near the curves: 1—LFW, 2—IFW, 3—HFW.

The distributions of the complex amplitudes for the incident pulses are chosen as:

$$A_{j0}(t) = A_{j0} \exp(-(t - 0.5L_t)^2), j = 1, 2, 3. \tag{16}$$

The intensities of LFW and HFW are satisfied to equality:  $|A_{10}|^2 + |A_{30}|^2 = 1$ . We also estimate the conversion efficiency via the following formula:



$$\eta_j = \frac{\int_0^{L_t} |A_j(z, t)|^2 dt}{\int_0^{L_t} (|A_1(0, t)|^2 + |A_2(0, t)|^2 + |A_3(0, t)|^2) dt}, j = 1, 2, 3.$$

#### 4.1. Frequency Conversion to Radiation with the Wavelength 4 μm

Here, we present the computer simulation results of the energy conversion from HFW to LFW, possessing wavelength 4 μm, occurring in the crystal AgGaS<sub>2</sub>. The SOD coefficients are chosen as follows:  $D_1 = -0.0002$ ,  $D_2 = -0.0125$ ,  $D_3 = -0.0217$ . So, the frequency of LFW is near the zero-dispersion point and the SOD of the HFW is a large one. In our notations, the negative sign of the SOD coefficient corresponds to the normal dispersion of a medium. The coefficient of nonlinear coupling  $\gamma$  is chosen equal to unity, which is achieved at a value of 6.12 GW/cm<sup>2</sup> of the sum intensity of the incident pulses.

##### 4.1.1. Incident IFW's Intensity Is Equal to Zero

We begin our consideration from the case for which a non-zero value of the intensities of incident LFW and HFW takes place (of course, the HFW possesses much more energy, than LFW), meanwhile, the intensity of incident IFW is absent:  $|A_{20}|^2 = 0$ . In this case, we analyze an influence of the intensity ratios between LFW and HFW on the effectiveness of energy conversion.

First, we consider the positive phase mismatching between LFW and IFW ( $\Delta_{21}k = 20$ ). Figure 2 presents the computer simulation results for various maximal intensities of the incident LFW:  $|A_{10}|^2 = 0.05, 0.07, 0.08, 0.1$ . We emphasize that the first two values of the intensity lead to the low-effective mode of the frequency down-conversion, and the two last values—to its high-effective mode.

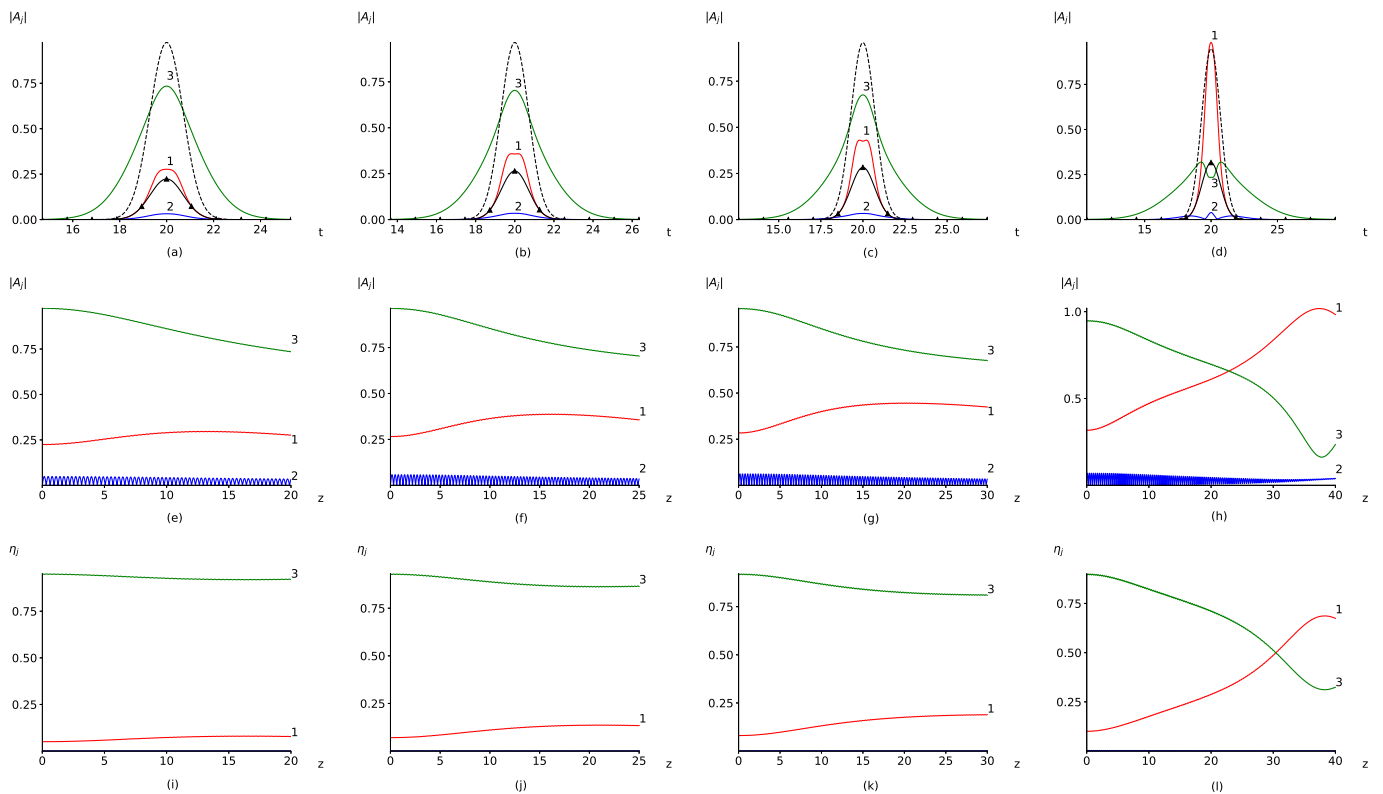


**Figure 2.** Pulses' shapes in the sections  $z = 20$  (a),  $25$  (b),  $30$  (c),  $40$  (d); pulse intensity evolution at their centers (e–h), and the frequency conversion efficiency evolution (i–l) along the  $z$ -coordinate computed for  $|A_{10}|^2 = 0.05$  (a,e,i),  $0.07$  (b,f,j),  $0.08$  (c,g,k),  $0.1$  (d,h,l).

Indeed, at the incident intensity  $|A_{10}^2| = 0.05$ , there is no remarkable frequency conversion between HFW and LFW (Figure 2i):  $\eta_1$  grows from 5% only to 7%. The LFW intensity at the pulse center also grows a little bit (Figure 2e). As for the shapes of the pulses (Figure 2a), the LFW pulse shape becomes flatter than the initial one, and the HFW pulse decompresses due to the SOD influence. Moreover, a weak IFW generation occurs (as it is supposed to).

The same situation is practically observed in the two next cases. At  $|A_{10}|^2 = 0.07$ , the frequency conversion is slightly more effective:  $\eta_1$  grows two times; from 7% to 15% (Figure 2j). Other peculiarities, such as the LFW intensity growth at the pulse center (Figure 2f), flattening of the LFW pulse shape, the HFW pulse decompression, and weak IFW generation (Figure 2b), are conserved. The incident intensity  $|A_{10}|^2 = 0.08$  does not experience enough improvement of the frequency down-conversion ( $\eta_1$ , achieving only 19% (Figure 2k)) in contrast to those achieved in the framework of the long-duration pulse approximation.

The explosive increasing frequency conversion efficiency occurs at  $|A_{10}|^2 = 0.1$ . In this case, the LFW intensity at the pulse center (Figure 2h) rises much faster than in all previous cases and even achieves the incident HFW intensity. Moreover, the LFW pulse (Figure 2d) is a bit more narrow than the incident HFW one. Thus, the resulting frequency conversion is very impressive: more, than 69% of the sum energy transfers to LFW (Figure 2l). It is worth noting that the HFW pulse has a local minimum near the pulse center, in this case (Figure 2d).

If we take into account the GVDs of the optical pulses, then a sign of the phase mismatching  $\Delta_{21}k$  will influence the conversion efficiency. So, if we choose a negative ( $\Delta_{21}k = -20$ ), then the situation changes, essentially because an action of a medium leads to decompression of the interacting pulses due to changing of the effective nonlinear response (see above:  $\tilde{\alpha} = \gamma^2/\Delta_{21}k$ ). Because the GVD coefficient  $D_1$  of the LFW is considerably small, this pulse undergoes decompression very weakly. As a consequence, the energy from the central part of the HFW converts to the energy of LFW, and the LFW intensity at the pulse center becomes larger than those occurring for  $\Delta_{21}k = 20$  (compare Figure 3e–h with Figure 2e–h). However, the pulse of HFW spreads faster, and most of it locates out of the time interval in which two other pulses are located. Consequently, no remarkable frequency conversion occurs far from the pulse centers. Thus, the HFW pulse possesses a local minimum near the pulse center in all cases (Figure 3a–d) despite the LFW pulse being smooth, with a small duration in comparison with the HFW pulse duration. The conversion efficiency is larger in the first three cases (18%, 34%, 38% in Figure 3i,j,k, correspondingly), but lower for the incident intensity of the LFW equal to  $|A_{10}|^2 = 0.1$  than the one occurring for the positive phase mismatching:  $\Delta_{21}k = 20$  (only 43%).

#### 4.1.2. Incident LFW's Intensity Is Equal to Zero

Below, we briefly discuss peculiarities of the frequency down-conversion if the incident LFW intensity is equal to zero ( $|A_{10}|^2 = 0$ ), and the intensity of the incident IFW is non-zero ( $|A_{20}|^2 = 0.4$ , for instance). In this case, at  $\gamma = 1$ , a much longer distance ( $z = 80$ ) of the pulses' interaction is required for the LFW generation. Obviously, the required distance can be decreased by the incident intensity increasing. For example, at  $\gamma = 2$ , the distance decreases five times, but the frequency down-conversion occurs in the same way as at  $\gamma = 1$ : there are no improvements in the pulse shapes.

The main feature of the interactions of the pulses involve developing their instability, which destroys the pulse shapes. Therefore, this scheme involving the pulse interactions at chosen parameters cannot be effectively used.

As above, a sign of the phase mismatching  $\Delta_{21}k$  remarkably influences the frequency down-conversion process, but the pulse shapes do not remain smooth. If  $\Delta_{21}k$  is positive, then the IFW energy converts partially to the LFW's one. The conversion efficiency of the frequency down-conversion is about 24%. If the phase mismatching between LFW and

IFW is negative, then the LFW generation is weaker than in the previous case ( $\eta_1 = 0.12$ ), and the IFW amplification occurs.

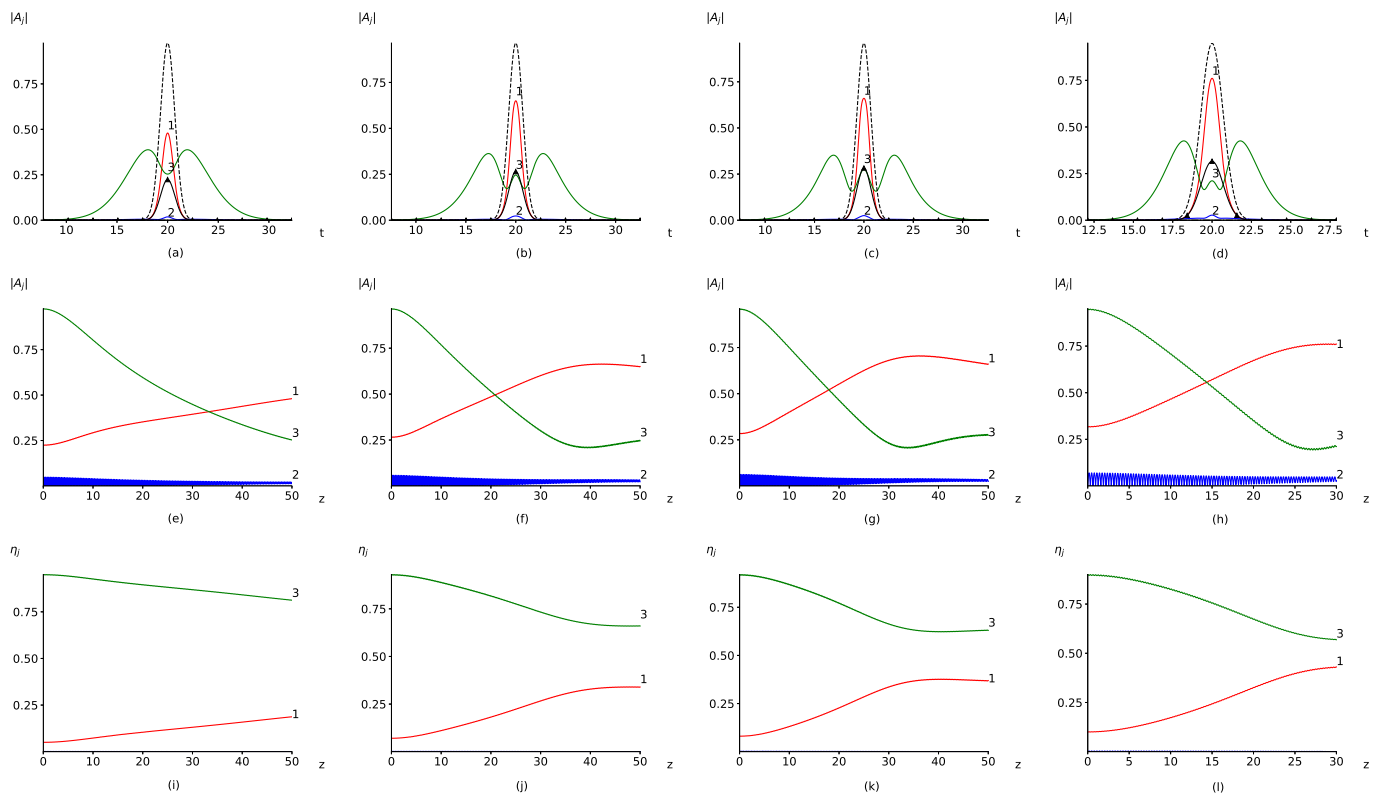


**Figure 3.** Pulse shapes in the section  $z = 50$  (a–c),  $30$  (d); pulse intensity evolution at the centers (e–h), and the frequency conversion efficiency evolution (i–l) along the  $z$ -coordinate computed for  $|A_{10}|^2 = 0.05$  (a,e,i),  $0.07$  (b,f,j),  $0.08$  (c,g,k),  $0.1$  (d,h,l).

It should be noted that, in contrast to the frequency conversion in the crystal  $\text{AgGaS}_2$ , for the tellurium crystal, we observe a completely different situation, as one can see below.

#### 4.2. Frequency Conversion to Radiation with the Wavelength $10 \mu\text{m}$

If the LFW’s wavelength equals  $10 \mu\text{m}$ , then the dimensionless SOD coefficients are equal to  $D_1 = 0.1633$ ,  $D_2 = 0.0755$ ,  $D_3 = -0.0414$  for the crystal  $\text{AgGaS}_2$ , respectively. Thus, the HFW undergoes a normal dispersion, and the LFW and IFW undergo anomalous ones. In this case, LFW amplification is not monotonic as in the previous case.

A significant increase of the conversion efficiency can be achieved by increasing the nonlinear coupling coefficient  $\gamma$  up to 4 to decrease the crystal length. In this case, the sum incident pulses intensity has to equal  $330 \text{ GW}/\text{cm}^2$ , keeping in mind the changing of the wavelength, increasing the coefficient  $\gamma$ , and changing the quadratic susceptibility due to changing the wavelength. It should be noted that this value is relatively high and perhaps requires an account for the influence of the third-order susceptibility on the three pulse interactions. Our computation shows that the dimensionless third-order nonlinear coefficient is equal to 0.02 in the case under consideration. Therefore, analyzing laser pulse interactions in short distances, the third-order nonlinear effects can be neglected.

The computer simulation results are depicted in Figure 4 for the phase mismatching between IFW and LFW equaling  $\Delta_{21}k = 22$ .

As one can see, there is a very effective generation of the IFW, although this wave is not phase-matched with two other waves in this case (Figure 4a). The LFW amplification efficiency achieves 41% and the intensive energy conversion to this wave occurs between sections  $z = 2$  and  $z = 3$ , including the explosive energy conversion of the interacting waves. Then the energy exchange between the interacting waves becomes very small.

Unfortunately, the pulse shapes have many local maxima and minima, which make the use of this mode of wave interactions for the frequency down-conversion impossible, in practice. It should be stressed that at a smaller incident intensity of the LFW ( $|A_{10}|^2$ ), the process of the frequency conversion takes place in the same manner, but with lower efficiency.

There is a similar conclusion with the LFW. The pulse shapes are also not smooth, and the HFW energy transfers to both LFW and IFW (Figure 4b). As a result, the frequency down-conversion efficiency achieves 21%.

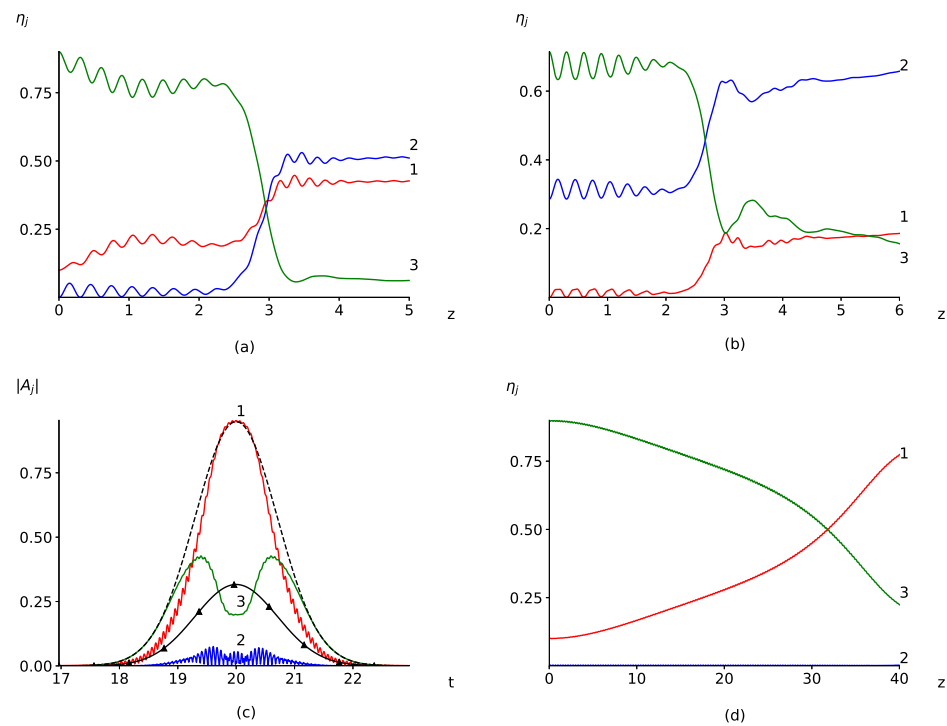


**Figure 4.** An evolution of the frequency conversion efficiency (a,b,d) along the  $z$ -coordinate and pulse shapes in the section  $z = 40$  (c) computed for  $(\gamma, |A_{10}|^2, |A_{20}|^2) = (4, 0.1, 0)$  (a),  $(4, 0, 0.4)$  (b),  $(1, 0.1, 0)$  (c,d).

The quality of the pulse shape and the frequency conversion efficiency can be sufficiently improved by increasing the incident pulse duration, for instance, until  $\tau_p = 1$  ps. This leads to decreases in the dimensionless GVD coefficients, for 100 times, and allows us to avoid developing the modulation instability of the pulses (Figure 4c,d). We see in this figure that even at a smaller value of the nonlinear coupling coefficient ( $\gamma = 1$ ) corresponding to the incident intensity  $20.66 \text{ GW/cm}^2$ , the conversion efficiency achieves a value of about 76% (Figure 4d). However, it requires increasing the length of the crystal: about 4 cm.

#### 4.3. Frequency Conversion to Radiation with the Wavelength to $24 \mu\text{m}$

Finally, we consider the frequency down-conversion process in a tellurium crystal at the incident pulse duration, 100 fs, which results in radiation generation with a frequency of 12.5 THz, corresponding to a wavelength of  $24 \mu\text{m}$ . The phase mismatching between IFW and LFW is small:  $\Delta_{21}k = 5.2$ . Therefore, the multi-scale method can give non-adequate results. However, some features of those analyses remain valid. The dimensionless SOD coefficients are also large, especially at the wavelength  $24 \mu\text{m}$  ( $D_1 = 0.218, D_2 = -0.079, D_3 = -0.154$ ). Consequently, we chose the coefficient of nonlinear coupling equal  $\gamma = 2$ . Due to the large value of the quadratic susceptibility  $\chi^{(2)}$  of the tellurium crystal, the corresponding sum intensity of the incident pulse can be small enough:  $110 \text{ MW/cm}^2$ . The computer simulation results are shown in Figure 5.

As one can see, the high- and low-effective modes of the frequency conversion can be observed in this figure. At the incident intensity  $|A_{10}|^2 = 0.07$  of the LFW, its energy changes from 7% to 34% (Figure 5g) and the pulse duration is about 200 fs (Figure 5a), which approximately corresponds to three periods of wave phase changes. Meanwhile, if the incident intensity slightly increases, up to  $|A_{10}|^2 = 0.08$ , then the conversion efficiency  $\eta_1$  achieves more than 82% (Figure 5h) and the pulse duration becomes equal, at about 500 fs (Figure 5b), which approximately corresponds to eight periods of wave phase changes. It is very important for practice that the LFW pulse shape is rather smooth (Figure 5a,b) in contrast to the two other waves.

If the incident LFW intensity is equal to zero, then the conversion efficiency achieves about 21% (Figure 5i) and the pulse duration is about 250 fs (Figure 5c), which corresponds to 4.5 periods of wave phase changes, approximately. However, the LFW pulse shape contains some local maxima and local minima. Nevertheless, its shape is smooth enough (Figure 5c).

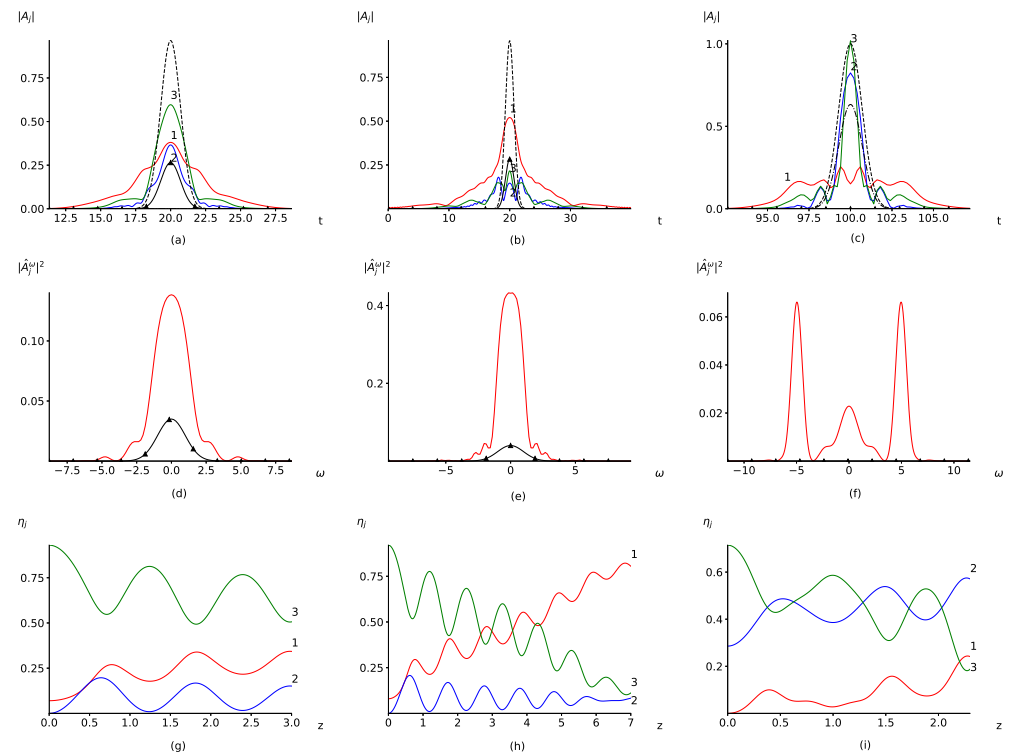


**Figure 5.** Pulse shapes in the section  $z = 3$  (a), 7 (b), 2.5 (c), and the LFW Fourier spectrum (d–f), and the frequency conversion efficiency evolution (g–i) along the  $z$ -coordinate computed for  $(|A_{10}|^2, |A_{20}|^2) = (0.07, 0)$  (a,d,g),  $(0.08, 0)$  (b,e,h),  $(0, 0.4)$  (c,f,i).

In Figure 5d–f, we depict the spectrum of the LFW. In the first two cases (Figure 5d,e), the LFW spectrum is smooth and broadened compared to the incident pulse. Regarding the LFW generation from its incident zero-value intensity (Figure 5f), the LFW spectrum has three local maxima. Thus, one could analyze the three sub-pulses, as could be seen in Figure 5c; they overlap each other in the time-domain.

The chirps of the incident pulses:

$$A_{j0}(t) = A_{j0} \exp(-(t - 0.5L_t)^2 + ic_j(t - 0.5L_t)^2), j = 1, 2, 3$$

can partially improve the frequency down-conversion efficiency. Above  $c_j$  equals to  $-1$ ,  $1$ , or  $0$ . We made a series of the computer simulations for the parameters:  $|A_{10}|^2 = 0.07$ ,  $|A_{20}|^2 = 0$ ,  $\gamma = 2$ ,  $\Delta_{21}k = 5.2$ ,  $D_1 = 0.218$ ,  $D_2 = -0.079$ ,  $D_3 = -0.154$ , at which the frequency down-conversion is relatively small; a quality of the pulse shape is bad for

non-chirped pulses (see Figure 5a,d,g). For comparison, the computer simulation results are presented in Figure 6.

It should be noted that both the up-chirping ( $c_3 = 1$ , Figure 6a,d,g) and the down-chirping ( $c_3 = -1$ , Figure 6b,e,h) of the HFW pulse lead to sufficient improvements of the frequency down-conversion efficiency—about 70% is achieved in both cases (compared with the 34% conversion efficiency in Figure 5g). However, there are some differences between these two cases of the LFW generation. The mentioned conversion efficiency is achieved for the down-chirped HFW pulse in a two-times smaller distance ( $z = 5$ ) than the corresponding value occurring for the up-chirped pulse of the HFW ( $z = 10$ ). If the pulse chirp is  $c_3 = 1$ , then the pulse shapes are smoother (Figure 6a) and do not possess the local minima, which can be observed in Figure 6b for IFW and HFW. However, the LFW pulse spectrum is broadened if the incident pulse possesses down-chirp ( $c_3 = -1$ ): the remarkable response of a medium can be observed in the pulse spectrum up to dimensionless frequencies  $\omega = \pm 6$  in Figure 6e, meanwhile, the LFW pulse spectrum almost vanishes at the frequency  $\omega = \pm 3$  in Figure 6d.

The effective LFW amplification also occurs if both the LFW and HFW possess down-chirps  $c_1 = -1, c_3 = -1$  in the input section  $z = 0$  (Figure 6c,f,i). In general, the frequency conversion process in this case is similar to those occurring for the pulse chirps  $c_1 = 0, c_3 = -1$  (Figure 6b,g,h). Only a slightly longer distance  $z = 6$  is required to achieve the high efficiency of the frequency conversion (Figure 6h) and a more pronounced spectral response occurs at a range of the dimensionless frequencies  $\omega = \pm(2.5 - 6.5)$  (Figure 6f).

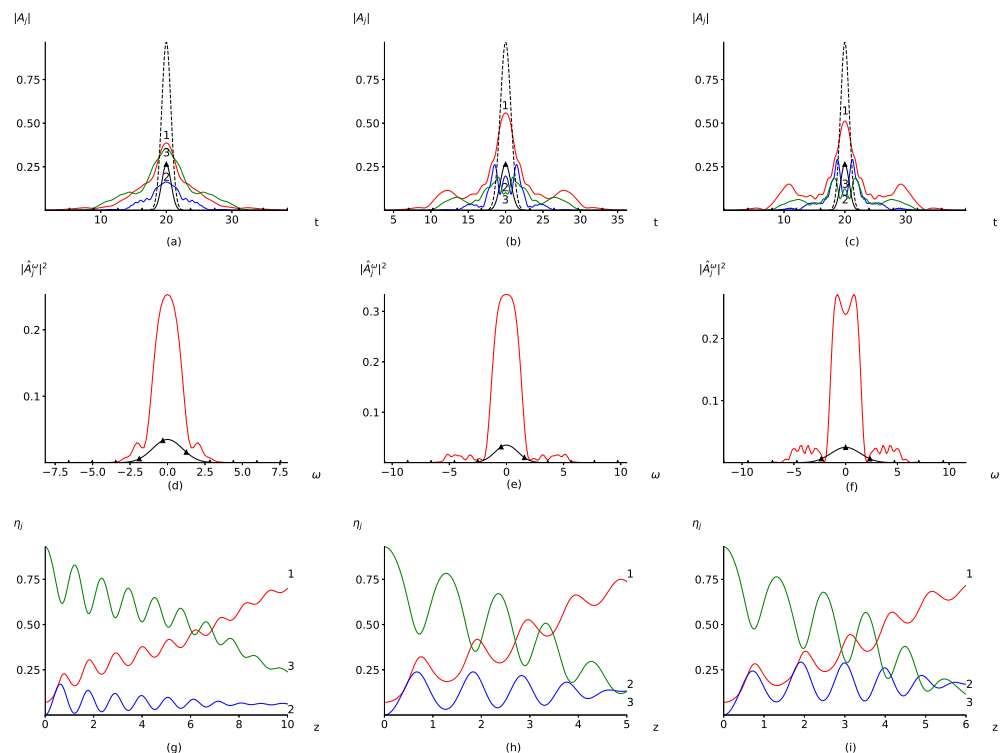


**Figure 6.** Pulse shapes in the section  $z = 10$  (a),  $5$  (b),  $6$  (c), corresponding to the LFW Fourier spectrum (d–f) and the frequency conversion efficiency evolution (g–i) along the  $z$ -coordinate computed for  $(c_1, c_2, c_3) = (0, 0, 1)$  (a,d,g),  $(0, 0, -1)$  (b,e,h),  $(-1, 0, 1)$  (c,f,i).

### 5. Discussion and Conclusions

We propose using the cascading process for frequency down-conversion to the mid-infrared (or even THz) range, due to wave generation with difference frequency at multiple frequencies of the interacting pulses. We showed that this method is applicable for frequency down-conversion corresponding to a wavelength of at least  $24 \mu\text{m}$ , but this is not a strict ‘upper bound’.

In the framework of a multi-scale method, we derived a set of modified equations and solved these equations without using the energy non-depletion approximation of the pump wave. This solution was supported by numerical experiments.

Influence of the GVD—of the pulses on the frequency down-conversion efficiency—was examined. The computer simulation results showed that non-zero incident LFW's energy could be amplified from an initial value of 8% to 75% and the LFW generation with 25% conversion efficiency is possible at the zero-value its incident intensity. It is important (for practice) that the pulse with a larger wavelength possesses a smooth shape and that its spectrum is also smooth.

Chirping of the incident HFW pulse could increase the conversion efficiency if the pulse chirp is chosen in an appropriate way. The significant increasing is observed for both up- and down-chirping of the pulse.

Concerning the possible experimental setup, based on data from Table 1 and computer simulation results—for the amplification of the optical pulse with the wavelength 4  $\mu\text{m}$ , we suggest the following configuration: two pulses, approximately with 100 fs durations, and the intensities of 0.612  $\text{GW}/\text{cm}^2$  (10% of the sum intensity) and 5.508  $\text{GW}/\text{cm}^2$  (90% of sum intensity), with wavelengths  $\lambda_1 = 4 \mu\text{m}$  (75 THz) and  $\lambda_3 \approx 1.333 \mu\text{m}$  (225 THz), respectively, fall on the  $\text{AgGaS}_2$  crystal with the length 4 cm, cut at an angle  $49.46^\circ$ .

For amplification of the optical pulse with 10  $\mu\text{m}$  wavelength, the crystal cut angle should be changed to  $79.51^\circ$ . The duration of the pulses should be increased until 1 ps and the intensities between them should be distributed in the following way: 2.066  $\text{GW}/\text{cm}^2$  for the pulse with the wavelength  $\lambda_1 = 10 \mu\text{m}$  (30 THz) and 18.54  $\text{GW}/\text{cm}^2$  for the pulse with the wavelength  $\lambda_3 \approx 3.333 \mu\text{m}$  (90 THz).

The experimental setup for a pulse generation with the wavelength 24  $\mu\text{m}$  can be implemented in the following way: the Te crystal, 2.5 mm in length, should be cut at an angle,  $15.78^\circ$ . Two pulses with 100 fs duration and with intensities of 0.44  $\text{GW}/\text{cm}^2$  at the wavelength  $\lambda_3 = 8 \mu\text{m}$  (37.5 THz) and 0.176  $\text{GW}/\text{cm}^2$  at the wavelength  $\lambda_2 = 12 \mu\text{m}$  (49 THz) should 'fall' on the crystal.

For the frequency down-conversion of the radiation with a wavelength  $\lambda = 1.3$  (or 1.1)  $\mu\text{m}$  to the wavelength  $\lambda = 24$  (or 30)  $\mu\text{m}$ , we propose, for example, two schemes (Figure 7) that allows us to reach the frequency 12.5 THz (Figure 7a) and 10 THz (Figure 7b), respectively. For this aim, it is necessary to use three crystals. In the first crystal ( $\text{AgGaS}_2$ ), a radiation with the tripled wavelength 4  $\mu\text{m}$  is generated. Then, the second similar crystal is used for the generation of a radiation with the wavelength 8  $\mu\text{m}$  or 10  $\mu\text{m}$ . The generation of the radiation with wavelength 24  $\mu\text{m}$  or 30  $\mu\text{m}$  occurs in the third crystal (Te or  $\text{Cs}_2\text{HgI}_2\text{Cl}_2$ ).

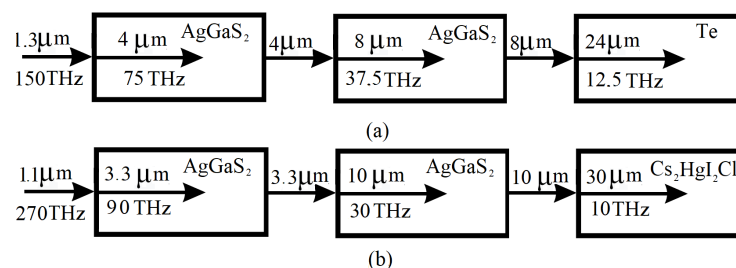


**Figure 7.** Two possible schemes of the frequency down-conversion to the THz range of the frequencies.

In above consideration, we did not take into account the absorption of laser radiation because our aim was a study of a maximal efficiency of the down-frequency based on the cascaded processes. If this efficiency was to be small, then, evidently, it would not make sense to consider other physical factors that decrease its effectiveness. One of these factor is the crystal's absorption of the laser radiation in the far IR and THz range of frequencies. Two crystals, used in our computer simulation, possess the following absorption coefficients for the radiation with wavelengths 4 mm and 10 mm: about  $1.2 \text{ cm}^{-1}$  for the crystal  $\text{AgGaS}_2$  [44]; and for the radiation with wavelength 24 mm: about  $1.7 \text{ cm}^{-1}$

for the crystal Te [36]. In dependence of a ratio between the intensities of the incident pulses the required crystals' lengths can change in the interval (2 mm, 7 mm) or even longer if the nonlinear coupling coefficient  $\gamma$  is equal to unity. To decrease the absorption of the laser energy, one can increase the intensity of the incident pulses that it is possible because we used the low-intensive pulses. In this case, we can decrease the crystal length in two or even more times. Moreover, there is other possibility to decrease the laser energy losses caused by the absorption by the crystals. At present time, many new nonlinear crystals were developed and they are transparent up to the wavelength 31  $\mu\text{m}$  ( $\text{Cs}_2\text{Hg}_3\text{I}_8$ , [45]), 41  $\mu\text{m}$  ( $\text{Cs}_2\text{HgI}_2\text{Cl}_2$ , [46]), respectively, or even 50  $\mu\text{m}$  (6 THz,  $\text{Cs}_2\text{Hg}_2\text{Br}_2\text{I}_4 \cdot \text{H}_2\text{O}$ , [47]) (full review of this research can be seen in [48]).

It should be mentioned that there are various IR laser, such as  $\text{CO}_2$  lasers with the wavelength 10.6  $\mu\text{m}$  and the duration 200 ns [49], the fiber lasers with the wavelength 3.9  $\mu\text{m}$  and with the pulse duration 160 fs with maximal power 200 kW [50,51], the quantum cascade laser that can generate a pulse with the wavelength  $\lambda_1 = 8 \mu\text{m}$  and with the pulse duration up to 630 fs possessing maximal power  $\max P(t)$  about of 4.5 W [52] and some others. Our scheme of the frequency down-conversion allows us to obtain the pulse with shorter duration and various wavelength and possessing broadband spectrum and with much high power density. Therefore, this scheme supplements the existence sources of the IR radiation and can be used for a generation of the THz broadband pulse.

Additional remark about the application of the converted frequency to the THz of the frequencies. As a rule, the THz radiation refers to the range of frequencies belonging to interval 0.1–10 THz. Figure 7 illustrates how one can reach this frequency range by using proposed approach. One can also use the quantum cascade laser and sources of the IR pulsed radiation and the chosen crystal for the frequency down-conversion. We emphasize that the many dangerous substances have the absorption frequencies in the range of the frequencies 10–20 THz (see, for example, [53], Table 1 in [54], Table 9.1 in [55], Figure 1 in [56]). Evidently, that these frequencies can be used for the problem of the detection and identification of such substances that is very important for practice. Thus, the proposed scheme of the frequency down-conversion can be covered this frequency range.

**Author Contributions:** V.A.T.: conceptualization, methodology, writing—review and editing, supervision, discussion; D.M.K.: software, investigation, writing—original draft, discussion; M.V.F.: formal analysis, discussion; Y.Y.: discussion, draft writing. All authors have read and agreed to the published version of the manuscript.

**Funding:** This research was funded by Key Program of Joint Fund of the National Natural Science Foundation of China (U2001218); International (regional) Cooperation and Exchange Program of the National Natural Science Foundation of China (51875215).

**Institutional Review Board Statement:** Not applicable.

**Informed Consent Statement:** Not applicable.

**Data Availability Statement:** All available data is within the paper.

**Conflicts of Interest:** The authors declare no conflict of interest.

## Appendix A

Below, we derive the equation set (9) that describes the frequency conversion process at large phase-mismatching between IFW and LFW:  $|\Delta_{21}k| \gg \gamma$ . In this case, the process of the optical pulse interactions possess various spatial scales: in particular, a small scale, defined by large-phase mismatching  $|\Delta_{21}k|$ , and a long spatial scale defined by the smallest dispersion length of the interacting pulses. Thus, we introduce a small parameter  $\mu = \frac{1}{\Delta_{21}k}$  and introduce various scales along the  $z$  coordinate: a small scale equal to the inverse phase-mismatching length:  $\xi = \frac{z}{\mu}$  and large longitudinal scales  $z_l = \mu^l z$ ,  $l = 0, 1, 2, \dots$ . Therefore, the complex amplitudes are expanded in a power series of  $\mu$ :



$$\begin{aligned}
 A_1 &= U + \mu U_1 + \mu^2 U_2 + \dots, \\
 A_2 &= V + \mu V_1 + \mu^2 V_2 + \dots, \\
 A_3 &= W + \mu W_1 + \mu^2 W_2 + \dots
 \end{aligned}
 \tag{A1}$$

Obviously, the functions in (A1) depend on all variables  $(t, \zeta, z_l | l \geq 0)$ . Then, we transform the differential operators using new variables:

$$\begin{aligned}
 L_j &= \frac{\partial}{\partial z} + v_{j1} \frac{\partial}{\partial t} + iD_j \frac{\partial^2}{\partial t^2} = \frac{\partial \zeta}{\partial z} \frac{\partial}{\partial \zeta} + \sum_{l=0}^{\infty} \frac{\partial z_l}{\partial z} \frac{\partial}{\partial z_l} + iD_j \frac{\partial^2}{\partial t^2} = \frac{1}{\mu} \frac{\partial}{\partial \zeta} + \sum_{l=0}^{\infty} \mu^l \frac{\partial}{\partial z_l} + iD_j \frac{\partial^2}{\partial t^2} \\
 &= \frac{1}{\mu} \frac{\partial}{\partial \zeta} + L_j^0 + \mu \frac{\partial}{\partial z_1} + \mu^2 \frac{\partial}{\partial z_2} + \dots, j = 1, 2, 3.
 \end{aligned}
 \tag{A2}$$

Here, the operator  $L_j$  is defined by

$$L_j^{(0)} = \frac{\partial}{\partial z_0} + v_{j1} \frac{\partial}{\partial t} + iD_j \frac{\partial^2}{\partial t^2}.$$

Then, we substitute the representation (A1) of the complex amplitudes into the equation set (1), and keep terms with an order, which is greater than  $\mu^2$ :

$$\begin{aligned}
 &\frac{1}{\mu} \frac{\partial U}{\partial \zeta} + L_1^{(0)} U + \mu \frac{\partial U}{\partial z_1} + \frac{\partial U_1}{\partial \zeta} + \mu L_1^{(0)} U_1 + \mu \frac{\partial U_2}{\partial \zeta} + \\
 &+ i\gamma \left( U^* V e^{-i\zeta} + V^* W e^{i\zeta} + \mu \left( (U^* V_1 + U_1^* V) e^{-i\zeta} + (V^* W_1 + V_1^* W) e^{i\zeta} \right) \right) + O(\mu^2) = 0, \\
 &\frac{1}{\mu} \frac{\partial V}{\partial \zeta} + L_2^{(0)} V + \mu \frac{\partial V}{\partial z_1} + \frac{\partial V_1}{\partial \zeta} + \mu L_2^{(0)} V_1 + \mu \frac{\partial V_2}{\partial \zeta} + \\
 &+ i\gamma \left( U^2 e^{i\zeta} + 2U^* W e^{i\zeta} + \mu (2U U_1 e^{i\zeta} + (U^* W_1 + U_1^* W) e^{i\zeta}) \right) + O(\mu^2) = 0, \\
 &\frac{1}{\mu} \frac{\partial W}{\partial \zeta} + L_3^{(0)} W + \mu \frac{\partial W}{\partial z_1} + \frac{\partial W_1}{\partial \zeta} + \mu L_3^{(0)} W_1 + \mu \frac{\partial W_2}{\partial \zeta} + \\
 &+ 3i\gamma \left( UV e^{-i\zeta} + \mu (UV_1 + U_1 V) e^{-i\zeta} \right) + O(\mu^2) = 0.
 \end{aligned}
 \tag{A3}$$

Grouping the terms with respect to the power of  $\mu$ , we obtain the equations:

$$\frac{\partial U}{\partial \zeta} = \frac{\partial V}{\partial \zeta} = \frac{\partial W}{\partial \zeta} = 0,$$

corresponding to  $\frac{1}{\mu}$  of the power series. Consequently, the functions  $U, V$  and  $W$  do not depend on the fast changing coordinate  $\zeta$ . Therefore, these functions do not change at the small scale.

For the next order  $O(1)$  of the power series on  $\mu$ , we obtain the following set of equations:

$$\begin{aligned}
 L_1^{(0)} U + \frac{\partial U_1}{\partial \zeta} + i\gamma (U^* V e^{-i\zeta} + V^* W e^{i\zeta}) &= 0, \\
 L_2^{(0)} V + \frac{\partial V_1}{\partial \zeta} + i\gamma (U^2 e^{i\zeta} + 2U^* W e^{i\zeta}) &= 0, \\
 L_3^{(0)} W + \frac{\partial W_1}{\partial \zeta} + 3i\gamma UV e^{-i\zeta} &= 0.
 \end{aligned}
 \tag{A4}$$

The first terms in these equations do not depend on  $\zeta$ ; however, as other terms depend on this variable, we can separate equations into two parts. The first of them is written as

$$L_1^{(0)} U = L_2^{(0)} V = L_3^{(0)} W = 0.
 \tag{A5}$$

The functions  $U_1, V_1, W_1$  can be written solving the second system by integrating (A4), with respect to  $\zeta$  variable:

$$\begin{aligned} U_1 &= \gamma(U^*Ve^{-i\zeta} - V^*We^{i\zeta}) + u_1(t, z_0, z_1 \dots), \\ V_1 &= \gamma(-U^2e^{i\zeta} - 2U^*We^{i\zeta}) + v_1(t, z_0, z_1 \dots), \\ W_1 &= 3\gamma UVe^{-i\zeta} + w_1(t, z_0, z_1 \dots). \end{aligned} \tag{A6}$$

Here  $u_1, v_1, w_1$  are the functions of integration: they do not depend on the  $\zeta$ -coordinate. The equations with respect to these functions are derived below.

For the functions at the order  $O(\mu)$  of the power series, we obtain the following equations:

$$\begin{aligned} \frac{\partial U_2}{\partial \zeta} + L_1^{(0)}U_1 + \frac{\partial U}{\partial z_1} + i\gamma((U^*V_1 + U_1^*V)e^{-i\zeta} + (V^*W_1 + V_1^*W)e^{i\zeta}) &= 0, \\ \frac{\partial V_2}{\partial \zeta} + L_2^{(0)}V_1 + \frac{\partial V}{\partial z_1} + i\gamma(2UU_1e^{i\zeta} + (U^*W_1 + U_1^*W)e^{i\zeta}) &= 0, \\ \frac{\partial W_2}{\partial \zeta} + L_3^{(0)}W_1 + \frac{\partial W}{\partial z_1} + 3i\gamma(UV_1 + U_1V)e^{-i\zeta} &= 0. \end{aligned}$$

Using the representation (A6), this set of equations transforms into the form:

$$\begin{aligned} \frac{\partial U_2}{\partial \zeta} + \gamma(L_1^{(0)}(U^*V)e^{-i\zeta} - L_1^{(0)}(V^*W)e^{i\zeta}) + i\gamma^2(U^*v_1e^{-i\zeta} - V^2W^*e^{-2i\zeta} + u_1^*Ve^{-i\zeta} + V^*w_1e^{i\zeta} + v_1^*We^{i\zeta}) &= \\ - \left( \frac{\partial U}{\partial z_1} + i\gamma^2(-|U|^2U - 3U^*2W + 4U|V|^2 - 2U|W|^2) \right) - L_1^{(0)}u_1, \\ \frac{\partial V_2}{\partial \zeta} - \gamma(L_2^{(0)}(U^2)e^{i\zeta} + 2L_2^{(0)}(U^*W)e^{i\zeta}) + i\gamma^2(-2UV^*We^{2i\zeta} + 2Uu_1e^{i\zeta} + 2UV^*We^{i\zeta} + 2u_1^*We^{i\zeta} + 2U^*we^{i\zeta}) &= \\ - \left( \frac{\partial V}{\partial z_1} + 2i\gamma^2(4|U|^2 - |W|^2)V \right) - L_2^{(0)}v_1, \\ \frac{\partial W_2}{\partial \zeta} + 3\gamma L_3^{(0)}(UV)e^{-i\zeta} + 3i\gamma^2(Uv_1e^{-i\zeta} + U^*V^2 * e^{-2i\zeta} + u_1V_1e^{-i\zeta}) &= \\ - \left( \frac{\partial W}{\partial z_1} - 3i\gamma^2(U^3 + 2|U|^2W + |V|^2W) \right) - L_3^{(0)}w_1. \end{aligned}$$

As before, we can state that the right-hand sides of the equations are equal to zero because they do not depend on  $\zeta$ , in contrast to the left-hand sides of the equations. Thus, we write the equations

$$\begin{aligned} \frac{\partial U}{\partial z_1} + i\gamma^2(-|U|^2U - 3U^*2W + 4U|V|^2 - 2U|W|^2) &= -L_1^{(0)}u_1, \\ \frac{\partial V}{\partial z_1} + 2i\gamma^2(4|U|^2 - |W|^2)V &= L_2^{(0)}v_1, \\ \frac{\partial W}{\partial z_1} - 3i\gamma^2(U^3 + 2|U|^2W + |V|^2W) &= L_3^{(0)}w_1. \end{aligned}$$

Above, we separate terms that contain  $u_1, v_1, w_1$ . They belong to order  $O(\mu)$  in the representation (A1); meanwhile,  $U, V, W$  are of order  $O(1)$ , then one can once again separate the obtained equation into two parts:

$$\begin{aligned} \frac{\partial U}{\partial z_1} + i\gamma^2(-|U|^2U - 3U^*2W + 4U|V|^2 - 2U|W|^2) &= 0, \\ \frac{\partial V}{\partial z_1} + 2i\gamma^2(4|U|^2 - |W|^2)V &= 0, \\ \frac{\partial W}{\partial z_1} - 3i\gamma^2(U^3 + 2|U|^2W + |V|^2W) &= 0. \end{aligned} \tag{A7}$$

Consequently, the equations

$$\begin{aligned} L_1^{(0)} u_1 &= 0, \\ L_2^{(0)} v_1 &= 0, \\ L_3^{(0)} w_1 &= 0 \end{aligned} \tag{A8}$$

take place.

After returning to the original variables, ( $\xi = \Delta_{21} k z$ ,  $z_0 = z$ ,  $z_1 = z / \Delta_{21} k$ ,  $\frac{\partial}{\partial z} = \Delta_{21} k \frac{\partial}{\partial \xi} + \frac{\partial}{\partial z_0} + \frac{1}{\Delta_{21} k} \frac{\partial}{\partial z_1} + O((\Delta_{21} k)^{-2})$ ), we obtain the sets of Equations (5) and (6). In turn, the expansion series (A1) transforms into the form (4).

## References

1. Stuart, B.H. *Infrared Spectroscopy: Fundamentals and Applications*; John Wiley & Sons: Hoboken, NJ, USA, 2004.
2. Dexheimer, S.L. *Terahertz Spectroscopy: Principles and Applications*; CRC Press: Boca Raton, FL, USA, 2017.
3. Consolino, L.; Bartalini, S.; De Natale, P. Terahertz frequency metrology for spectroscopic applications: A review. *J. Infrared Millim. Terahertz Waves* **2017**, *38*, 1289–1315. [[CrossRef](#)]
4. Chen, H.; Chen, H.; Che, W.; Zheng, S.; Xiu, X.; Xue, Q. Review and modification of permittivity measurement on open resonator for transparent material measurements at terahertz. *IEEE Trans. Instrum. Meas.* **2020**, *69*, 9144–9156. [[CrossRef](#)]
5. Walsh, B.M.; Lee, H.R.; Barnes, N.P. Mid infrared lasers for remote sensing applications. *J. Lumin.* **2016**, *169*, 400–405. [[CrossRef](#)]
6. Erny, C.; Moutzouris, K.; Biegert, J.; Kühlke, D.; Adler, F.; Leitenstorfer, A.; Keller, U. Mid-infrared difference-frequency generation of ultrashort pulses tunable between 3.2 and 4.8  $\mu\text{m}$  from a compact fiber source. *Opt. Lett.* **2007**, *32*, 1138–1140. [[CrossRef](#)] [[PubMed](#)]
7. Devi, K.; Schunemann, P.; Ebrahim-Zadeh, M. Continuous-wave, multimilliwatt, mid-infrared source tunable across 6.4–7.5  $\mu\text{m}$  based on orientation-patterned GaAs. *Opt. Lett.* **2014**, *39*, 6751–6754. [[CrossRef](#)] [[PubMed](#)]
8. Cruz, F.C.; Maser, D.L.; Johnson, T.; Ycas, G.; Klose, A.; Giorgetta, F.R.; Coddington, I.; Diddams, S.A. Mid-infrared optical frequency combs based on difference frequency generation for molecular spectroscopy. *Opt. Express* **2015**, *23*, 26814–26824. [[CrossRef](#)]
9. Ruehl, A.; Gambetta, A.; Hartl, I.; Fermann, M.E.; Eikema, K.S.; Marangoni, M. Widely-tunable mid-infrared frequency comb source based on difference frequency generation. *Opt. Lett.* **2012**, *37*, 2232–2234. [[CrossRef](#)]
10. Hildenbrand, A.; Kieleck, C.; Lallier, E.; Faye, D.; Grisard, A.; Gérard, B.; Eichhorn, M. Compact efficient mid-infrared laser source: OP-GaAs OPO pumped by  $\text{Ho}^{3+}$ : YAG laser. In *Technologies for Optical Countermeasures VIII*; International Society for Optics and Photonics: Bellingham, WA, USA, 2011; Volume 8187, p. 81870H. [[CrossRef](#)]
11. Boyko, A.A.; Kostyukova, N.Y.; Badikov, V.; Badikov, D.; Panyutin, V.; Shevyrdyaeva, G.; Pasiskevicius, V.; Zukauskas, A.; Marchev, G.M.; Kolker, D.B.; et al. Intracavity difference-frequency mixing of optical parametric oscillator signal and idler pulses in  $\text{BaGa}_4\text{Se}_7$ . *Appl. Opt.* **2017**, *56*, 2783–2786. [[CrossRef](#)]
12. Cui, C.; Lu, D.; Liang, F.; Wang, J.; Yu, H.; Zhang, H. Mid-infrared pulsed nanosecond difference frequency generation of oxide LGN crystal up to 5.7  $\mu\text{m}$ . *Opt. Lett.* **2021**, *46*, 785–788. [[CrossRef](#)]
13. Petrov, V. Frequency down-conversion of solid-state laser sources to the mid-infrared spectral range using non-oxide nonlinear crystals. *Prog. Quantum Electron.* **2015**, *42*, 1–106. [[CrossRef](#)]
14. Kawase, K.; Sato, M.; Taniuchi, T.; Ito, H. Coherent tunable THz-wave generation from  $\text{LiNbO}_3$  with monolithic grating coupler. *Appl. Phys. Lett.* **1996**, *68*, 2483–2485. [[CrossRef](#)]
15. Sasaki, Y.; Avetisyan, Y.; Yokoyama, H.; Ito, H. Surface-emitted terahertz-wave difference-frequency generation in two-dimensional periodically poled lithium niobate. *Opt. Lett.* **2005**, *30*, 2927–2929. [[CrossRef](#)] [[PubMed](#)]
16. Wang, T.; Lin, S.; Lin, Y.; Chiang, A.; Huang, Y. Forward and backward terahertz-wave difference-frequency generations from periodically poled lithium niobate. *Opt. Express* **2008**, *16*, 6471–6478. [[CrossRef](#)] [[PubMed](#)]
17. Li, Z.; Sun, X.; Zhang, H.; Li, Y.; Yuan, B.; Jiao, B.; Zhao, J.; Tan, L.; Bing, P.; Wang, Z.; et al. High-efficiency terahertz wave generation in aperiodically poled lithium niobate by cascaded difference frequency generation. *JOSA B* **2020**, *37*, 2416–2422. [[CrossRef](#)]
18. Shi, W.; Ding, Y.J.; Ferneliuss, N.; Vodopyanov, K. Efficient, tunable, and coherent 0.18–5.27-THz source based on GaSe crystal. *Opt. Lett.* **2002**, *27*, 1454–1456. [[CrossRef](#)] [[PubMed](#)]
19. Shi, W.; Ding, Y.J. Continuously tunable and coherent terahertz radiation by means of phase-matched difference-frequency generation in zinc germanium phosphide. *Appl. Phys. Lett.* **2003**, *83*, 848–850. [[CrossRef](#)]
20. Shi, W.; Ding, Y.J. Tunable terahertz waves generated by mixing two copropagating infrared beams in GaP. *Opt. Lett.* **2005**, *30*, 1030–1032. [[CrossRef](#)]
21. Ding, Y.; Shi, W. Widely tunable monochromatic THz sources based on phase-matched difference-frequency generation in nonlinear-optical crystals: A novel approach. *Laser Phys.* **2006**, *16*, 562–570. [[CrossRef](#)]
22. Cronin-Golomb, M. Cascaded nonlinear difference-frequency generation of enhanced terahertz wave production. *Opt. Lett.* **2004**, *29*, 2046–2048. [[CrossRef](#)]

23. Danielson, J.; Jameson, A.; Tomaino, J.; Hui, H.; Wetzel, J.; Lee, Y.S.; Vodopyanov, K. Intense narrow band terahertz generation via type-II difference-frequency generation in ZnTe using chirped optical pulses. *J. Appl. Phys.* **2008**, *104*, 033111. [[CrossRef](#)]
24. He, Y.; Wang, Y.; Xu, D.; Nie, M.; Yan, C.; Tang, L.; Shi, J.; Feng, J.; Yan, D.; Liu, H.; et al. High-energy and ultra-wideband tunable terahertz source with DAST crystal via difference frequency generation. *Appl. Phys. B* **2018**, *124*, 16. [[CrossRef](#)]
25. Yan, D.; Wang, Y.; Xu, D.; Liu, P.; Yan, C.; Shi, J.; Liu, H.; He, Y.; Tang, L.; Feng, J.; et al. High-average-power, high-repetition-rate tunable terahertz difference frequency generation with GaSe crystal pumped by 2  $\mu\text{m}$  dual-wavelength intracavity KTP optical parametric oscillator. *Photonics Res.* **2017**, *5*, 82–87. [[CrossRef](#)]
26. Ding, Y.J. Progress in terahertz sources based on difference-frequency generation. *JOSA B* **2014**, *31*, 2696–2711. [[CrossRef](#)]
27. Fujita, K.; Jung, S.; Jiang, Y.; Kim, J.H.; Nakanishi, A.; Ito, A.; Hitaka, M.; Edamura, T.; Belkin, M.A. Recent progress in terahertz difference-frequency quantum cascade laser sources. *Nanophotonics* **2018**, *7*, 1795–1817. [[CrossRef](#)]
28. De Regis, M.; Consolino, L.; Bartalini, S.; De Natale, P. Waveguided approach for difference frequency generation of broadly-tunable continuous-wave terahertz radiation. *Appl. Sci.* **2018**, *8*, 2374. [[CrossRef](#)]
29. Elsaesser, T.; Lobentanzer, H.; Seilmeier, A. Generation of tunable picosecond pulses in the medium infrared by down-conversion in AgGaS<sub>2</sub>. *Opt. Commun.* **1985**, *52*, 355–359. [[CrossRef](#)]
30. Canarelli, P.; Benko, Z.; Curl, R.; Tittel, F.K. Continuous-wave infrared laser spectrometer based on difference frequency generation in AgGaS<sub>2</sub> for high-resolution spectroscopy. *JOSA B* **1992**, *9*, 197–202. [[CrossRef](#)]
31. Okorogu, A.; Mirov, S.; Lee, W.; Crouthamel, D.; Jenkins, N.; Dergachev, A.Y.; Vodopyanov, K.; Badikov, V. Tunable middle infrared downconversion in GaSe and AgGaS<sub>2</sub>. *Opt. Commun.* **1998**, *155*, 307–312. [[CrossRef](#)]
32. Golubovic, B.; Reed, M. All-solid-state generation of 100-kHz tunable mid-infrared 50-fs pulses in type I and type II AgGaS<sub>2</sub>. *Opt. Lett.* **1998**, *23*, 1760–1762. [[CrossRef](#)]
33. Haidar, S.; Nakamura, K.; Niwa, E.; Masumoto, K.; Ito, H. Mid-infrared (5–12- $\mu\text{m}$ ) and limited (5.5–8.5- $\mu\text{m}$ ) single-knob tuning generated by difference-frequency mixing in single-crystal AgGaS<sub>2</sub>. *Appl. Opt.* **1999**, *38*, 1798–1801. [[CrossRef](#)]
34. Cheng, M.; Wu, S.; Zhu, Z.Z.; Guo, G.Y. Large second-harmonic generation and linear electro-optic effect in trigonal selenium and tellurium. *Phys. Rev. B* **2019**, *100*, 035202. [[CrossRef](#)]
35. Knyazev, G.; Voloshinov, V. Diffraction of IR radiation by ultrasound in tellurium single crystals. *Bull. Russ. Acad. Sci. Phys.* **2008**, *72*, 1643–1647. [[CrossRef](#)]
36. Patel, C.K.N. Efficient Phase-Matched Harmonic Generation in Tellurium with a CO<sub>2</sub> Laser at 10.6  $\mu\text{m}$ . *Phys. Rev. Lett.* **1965**, *15*, 1027–1030. [[CrossRef](#)]
37. Bridges, T.; Nguyen, V.; Burkhardt, E.; Patel, C. Tunable cw difference-frequency generation in tellurium at 11  $\mu\text{m}$ . *Appl. Phys. Lett.* **1975**, *27*, 600–602. [[CrossRef](#)]
38. Fan, Y.X.; Eckardt, R.; Byer, R.; Route, R.; Feigelson, R. AgGaS<sub>2</sub> infrared parametric oscillator. *Appl. Phys. Lett.* **1984**, *45*, 313–315. [[CrossRef](#)]
39. Bhar, G.C. Refractive index interpolation in phase-matching. *Appl. Opt.* **1976**, *15*, 305–307. [[CrossRef](#)]
40. Boyd, R.W. *Nonlinear Optics*; Academic Press: Cambridge, MA, USA, 2020. [[CrossRef](#)]
41. Gordienko, V.M.; Grechin, S.S.; Ivanov, A.A.; Podshivalov, A.A. Highly efficient generation of second and third harmonics of a femtosecond Cr: forsterite laser in nonlinear optical crystals. *Quantum Electron.* **2005**, *35*, 525. [[CrossRef](#)]
42. Begishev, I.A.; Kalashnikov, M.; Karpov, V.; Nickles, P.; Schönagel, H.; Kulagin, I.A.; Usmanov, T. Limitation of second-harmonic generation of femtosecond Ti: sapphire laser pulses. *JOSA B* **2004**, *21*, 318–322. [[CrossRef](#)]
43. Trofimov, V.A.; Trofimov, V.V. High effective SHG of femtosecond pulse with ring profile of beam in bulk medium with cubic nonlinear response. In *Laser Optics 2006: Solid State Lasers and Nonlinear Frequency Conversion*; SPIE: Bellingham, WA, USA, 2007; Volume 6610, pp. 200–208. [[CrossRef](#)]
44. Singh, N.; Hopkins, R.; Feichtner, J. Effect of annealing on the optical quality of AgGaS<sub>2</sub> and AgGaSe<sub>2</sub> single crystals. *J. Mater. Sci.* **1986**, *21*, 837–841. [[CrossRef](#)]
45. Zhang, G.; Qin, J.; Liu, T.; Zhu, T.; Fu, P.; Wu, Y.; Chen, C. Synthesis, characterization, and crystal growth of Cs<sub>2</sub>Hg<sub>3</sub>I<sub>8</sub>: A new second-order nonlinear optical material. *Cryst. Growth Des.* **2008**, *8*, 2946–2949. [[CrossRef](#)]
46. Zhang, G.; Li, Y.; Jiang, K.; Zeng, H.; Liu, T.; Chen, X.; Qin, J.; Lin, Z.; Fu, P.; Wu, Y.; et al. A new mixed halide, Cs<sub>2</sub>HgI<sub>2</sub>Cl<sub>2</sub>: molecular engineering for a new nonlinear optical material in the infrared region. *J. Am. Chem. Soc.* **2012**, *134*, 14818–14822. [[CrossRef](#)] [[PubMed](#)]
47. Wu, Q.; Huang, Y.; Meng, X.; Zhong, C.; Chen, X.; Qin, J. Exploration of new second-order nonlinear optical materials of the Cs–Hg–Br–I system. *Dalton Trans.* **2014**, *43*, 8899–8904. [[CrossRef](#)] [[PubMed](#)]
48. Guo, S.P.; Chi, Y.; Guo, G.C. Recent achievements on middle and far-infrared second-order nonlinear optical materials. *Coord. Chem. Rev.* **2017**, *335*, 44–57. [[CrossRef](#)]
49. Smith, A.; Mellis, J. Operating efficiencies in pulsed carbon dioxide lasers. *Appl. Phys. Lett.* **1982**, *41*, 1037–1039. [[CrossRef](#)]
50. Schneide, J.; Carbonnier, C.; Unrau, U.B. Characterization of a Ho 3+-doped fluoride fiber laser with a 3.9- $\mu\text{m}$  emission wavelength. *Appl. Opt.* **1997**, *36*, 8595–8600. [[CrossRef](#)]
51. Duval, S.; Gauthier, J.C.; Robichaud, L.R.; Paradis, P.; Olivier, M.; Fortin, V.; Bernier, M.; Piché, M.; Vallée, R. Watt-level fiber-based femtosecond laser source tunable from 2.8 to 3.6  $\mu\text{m}$ . *Opt. Lett.* **2016**, *41*, 5294–5297. [[CrossRef](#)]
52. Täschler, P.; Bertrand, M.; Schneider, B.; Singleton, M.; Jouy, P.; Kapsalidis, F.; Beck, M.; Faist, J. Femtosecond pulses from a mid-infrared quantum cascade laser. *Nat. Photonics* **2021**, *15*, 919–924. [[CrossRef](#)]

53. Schmuttenmaer, C.A. Exploring dynamics in the far-infrared with terahertz spectroscopy. *Chem. Rev.* **2004**, *104*, 1759–1780. [[CrossRef](#)]
54. Liu, H.B.; Zhong, H.; Karpowicz, N.; Chen, Y.; Zhang, X.C. Terahertz spectroscopy and imaging for defense and security applications. *Proc. IEEE* **2007**, *95*, 1514–1527. [[CrossRef](#)]
55. Zhang, X.C.; Xu, J. *Introduction to THz Wave Photonics*; Springer: New York, NY, USA, 2010; Volume 29. [[CrossRef](#)]
56. Novelli, F.; Guchhait, B.; Havenith, M. Towards intense THz spectroscopy on water: Characterization of optical rectification by GaP, OH1, and DSTMS at OPA wavelengths. *Materials* **2020**, *13*, 1311. [[CrossRef](#)]